

Physical mechanisms for the transition from type-III to large ELMs induced by impurity injection on EAST

X. Lin^a, G.S. Xu^{a*}, Q.Q. Yang^{a*}, N. Yan^a, Y.F. Wang^a, Y. Ye^b, P. Zhu^{c,d}, B. Cao^a, K.D. Li^a, R. Chen^a, L. Zhang^a, Q. Zang^a, T. Zhang^a, Y.M. Wang^a, G.H. Hu^a, Y.Y. Li^a, C. Zhou^e, Y.J. Chen^a, L.Y. Meng^{a,e}, X.D. Yang^a, Y.M. Duan^a, H.Q. Liu^a, F. Ding^a, X.H. Chen^a, J.C. Xu^a, M.F. Wu^{a,e}, L. Wang^a and the EAST team^a

^a Institute of Plasma Physics, HFIPS, Chinese Academy of Sciences, Hefei 230031, China

^b Institute of Energy, Hefei Comprehensive National Science Center, Hefei 230031, China

^c International Joint Research Laboratory of Magnetic Confinement Fusion and Plasma Physics, State Key Laboratory of Advanced Electromagnetic Engineering and Technology, School of Electrical and Electronic Engineering, Huazhong University of Science and Technology, Wuhan, Hubei 430074, China

^d Department of Engineering Physics, University of Wisconsin-Madison, Madison, Wisconsin 53706, USA

^e University of Science and Technology of China, Hefei 230026, China

*Corresponding author: gsxu@ipp.ac.cn and yangqq@ipp.ac.cn

Abstract

Transition from type-III to large-amplitude ELMs induced by neon injection has been observed in the EAST tokamak at overlapping q_{95} space between large and small ELMs. With neon injection, pedestal density gradient shows a remarkable increase accompanied by some decrease of pedestal electron temperature, and consequently the pressure gradient increases moderately and edge bootstrap current has minimal change. Further experiment demonstrates that the occurrence of large ELMs after

neon injection is highly correlated with the change in edge density. Linear peeling-ballooning stability analysis indicates that the large ELM case is more unstable than the type-III ELM case during the ELM transition. A scan of pedestal density gradient in linear stability analysis shows that the direct destabilizing effect of steep pedestal density gradient on peeling-ballooning instabilities via two-fluid effects could also facilitate the transition to large ELMs. These results could provide more insight into the role of pedestal density gradient on pedestal stability and ELM behavior.

Keywords: impurity injection, ELMs, pedestal density gradient, EAST tokamak

1. Introduction

The high-confinement mode (H-mode), characterized by the steep pedestal region inside the separatrix, is the most promising scenario for future fusion reactors such as ITER [1] and CFETR [2]. The edge localized modes (ELMs) which cause a high power load on the main chamber wall and the divertor target bring a great challenge for the safe operation of future reactors in the H-mode scenario. When the transient heat loads of large-amplitude ELMs exceed the tolerable limit of plasma facing component (PFC) material, it will pose a significant risk of unacceptable erosion. Considering the detrimental effects of large ELMs on the tokamak operation, significant efforts have been made on ELM mitigation and control over the past decades.

External impurity injection has been proved to be an effective method to mitigate or suppress ELMs [3]. For instance, in the impurity injection experiments on JET with the carbon wall (JET-C), a transition from type-I to type-III ELMs has been observed with the increasing radiative power fraction [4], and similar ELM transition by using extrinsic impurity injection has also been achieved in JT-60U [5]. In the all-tungsten ASDEX-Upgrade tokamak, mitigation of type-I ELMs with the ELM phase labelled 'Ib' disappearing was observed by using nitrogen seeding [6]. With the application of lithium impurity, ELM suppression has been achieved in the DIII-D [7], NSTX [8] and EAST [9, 10] devices. In addition to ELM mitigation and suppression, different ELM responses to impurity injection can also be observed in experiments. In JET with the ITER-like wall (JET-ILW), the pedestal confinement and ELM energy loss decrease in contrast to the JET-C, however, when nitrogen impurity is seeded the ELM amplitude increases and reaches the energy loss comparable to the JET-C,

accompanying the partial recovery of pedestal confinement [11]. In HL-2A the neon (Ne) injection experiments indicate that the ELM behavior is sensitive to the impurity ratio of injected gas mixture [12], i.e. low Ne ratio leads to ELM mitigation or suppression, but pure Ne gas causes only the reduction of ELM frequency without significant change in ELM amplitude. Generally speaking, extrinsic impurity injection has a strong impact on the ELM activity, however the physics mechanisms behind it are complex that have not been fully understood yet.

In the past few years, supersonic molecular beam injection (SMBI) system was applied to impurity injection and radiative feedback control in the EAST tokamak [13] for its advantages of higher fuelling efficiency and faster response time relative to the conventional gas puffing [14]. Interestingly, in this experimental series, an anomalous transition from type-III ELMs to low-frequency large-amplitude ELMs was observed in the H-mode plasma with a short Ne impurity pulse. Note that this experiment was operated at overlapping q_{95} space between large and small ELMs (i.e. $q_{95} \sim 5.2-6.4$), and more significantly, the ELM transition between large and small ELMs was commonly observed in this overlapping q_{95} space with plasma parameter changing or other external methods on EAST. The impurity effects, including dilution effect, increased effective charge number Z_{eff} and lower separatrix temperature $T_{\text{e,sep}}$, are generally beneficial for the pedestal stability that could not contribute to the impurity-induced transition to large ELMs [15]. In order to explore the underlying mechanisms, the experimental analysis and numerical simulation with various magnetohydrodynamic (MHD) codes are performed in this paper. Our study indicates that, in addition to the effect from the moderate increase in pedestal pressure gradient, the direct destabilizing effect of a steep pedestal density gradient on low- n and intermediate- n peeling-ballooning (PB) instabilities via two-fluid effects could also contribute to the triggering of large ELMs after Ne injection.

The rest of this paper is organized as follows. Section 2 describes the impurity injection experiments with transition from type-III to large ELMs. The underlying mechanism for the anomalous transition to large ELMs is explored with numerical simulations in section 3. Further discussions about the effect of Z_{eff} variation on the pedestal stability and the correlation of ELM amplitude with pedestal density gradient are presented in section 4. Finally, a summary is given in section 5.

2. Impurity injection experiments in EAST

In the past few years, a series of impurity injection experiments have been

carried out on the EAST machine, which is a fully superconducting tokamak with major radius $R_0 = 1.88$ m and minor radius $a = 0.45$ m. The EAST tokamak has been equipped with an ITER-like tungsten upper divertor, a carbon lower divertor and molybdenum first wall. EAST has a flexible poloidal field control system to achieve upper single null (USN), lower single null (LSN) and double null divertor configurations. In the following, the Ne injection experiment with anomalous transition from type-III to large ELMs is described in detail.

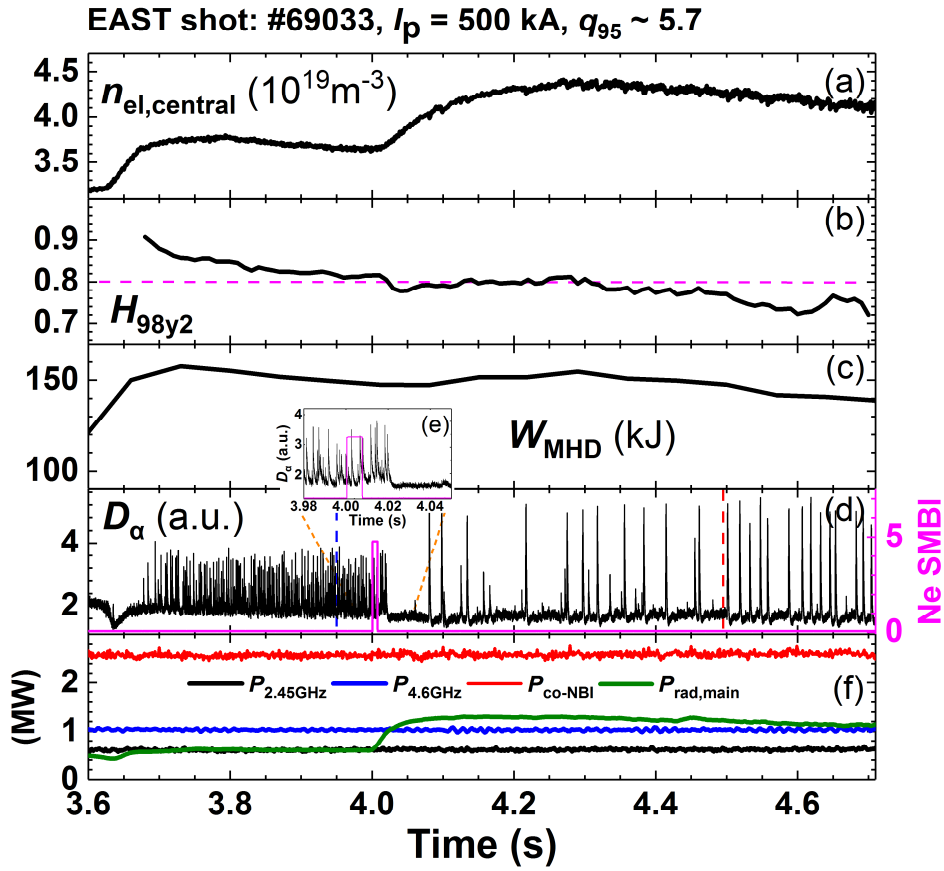


Fig. 1. Time traces for discharge #69033 of (a) central line-averaged density $n_{el,central}$, (b) confinement enhancement factor H_{98y2} , (c) stored energy W_{MHD} , (d) divertor D_α emission and monitor of the SMBI pulse, (e) the zoom in on D_α emission from 3.98 s to 4.05 s, (f) source heating power and radiated power $P_{rad,main}$. In the discharge, a pure Ne gas pulse of 7 ms is injected into the plasma from outer midplane by SMBI at 4 s.

Fig. 1 shows the typical impurity injection discharge #69033 under type-III ELMy H-mode background plasma at plasma current $I_p = 500$ kA, toroidal field $B_t \sim 2.5$ T, low poloidal beta $\beta_p \sim 0.9$, edge safety factor $q_{95} \sim 5.7$, upper triangularity $\delta_u =$

0.5 and elongation $\kappa = 1.62$ in the USN configuration. It is worth noting that the q_{95} in this discharge is in the overlapping q_{95} space between large and small ELMs (i.e. $q_{95} \sim 5.2-6.4$) where both large and small grassy ELMs could coexist [16]. The source heating power is relatively low, including 0.6 MW 2.45 GHz lower hybrid current drive (LHCD), 1 MW 4.6 GHz LHCD and 2.6 MW co-current neutral beam injection (NBI). In this discharge, a pure Ne gas pulse is injected into the plasma from outer midplane by SMBI at $t = 4$ s with Ne particle injection rate $\Gamma_{\text{Ne}} \sim 5 \times 10^{21}$ /s, and the pulse width is 7 ms.

The most important experimental phenomenon in the discharge is the ELM transition from type-III to low-frequency large ELMs, as shown in Fig. 1(d). Before Ne injection, the plasma is performed in type-III ELMy H-mode regime with ELM frequency $f_{\text{ELM}} \sim 500$ Hz. In contrast, after Ne injection the ELMs are first fully suppressed for about 60 ms. However, unexpectedly, the low-frequency large ELMs ($f_{\text{ELM}} \sim 55$ Hz) occur with the plasma density increasing dramatically from 3.6 to 4.2×10^{19} m^{-3} . The rapid reduction of divertor D_{α} emission (lasting ~ 2 ms) in Fig. 1(e) suggests that the particle flux transported from the main plasma to the divertor region is suddenly lower. This implies that the particle confinement may be improved after Ne injection. Note that, no significant degradation of plasma performance is observed with Ne injection that stored energy stays constant at $W_{\text{MHD}} \sim 150$ kJ ($H_{98y2} \sim 0.8$) though the radiated power in the main plasma modestly increases, which is desired for the impurity injection scenario in future reactors. The electron temperature T_{et} at strike point on the upper outer divertor decreases from ~ 20 eV to ~ 15 eV and there is no significant change in ion saturation current density j_s , indicating that the divertor target is still attached after Ne injection. Since the time resolution of Thomson Scattering system is low, the electron temperature profile in the short ELM-free phase cannot be available for pedestal stability analysis. Therefore this work mainly focuses on the physical mechanism for the triggering of large ELMs after Ne injection.

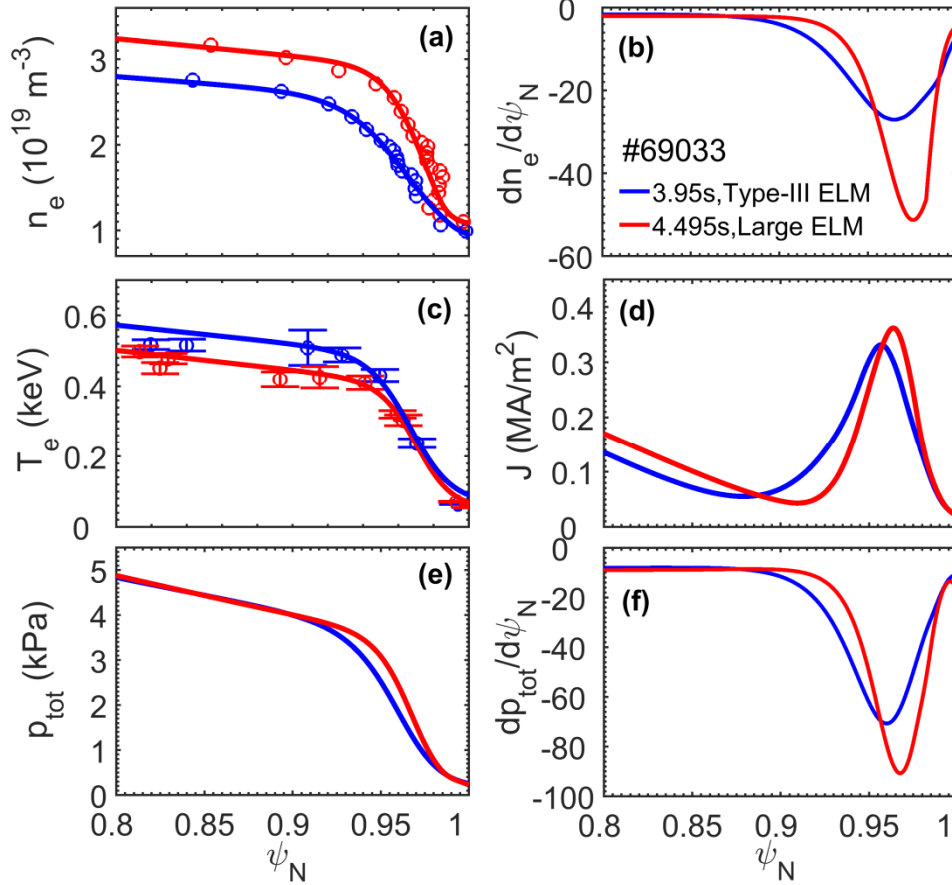


Fig. 2. Edge profiles of (a) electron density n_e , (b) density gradient $dn_e/d\psi_N$, (c) electron temperature T_e , (d) current density (e) total pressure and (f) pressure gradient for type-III ELM phase (blue line, $t = 3.95$ s) and large ELM phase (red line, $t = 4.495$ s) of discharge #69033. ψ_N is normalized poloidal flux.

The unexpected ELM response to Ne injection in the experiment could be highly related to the variations of pedestal profiles, as shown in Fig. 2. The electron density n_e and electron temperature T_e profiles, measured by microwave reflectometer [17, 18] and Thomson Scattering [19, 20] respectively, are well represented by the modified tanh function described in [21]. These plasma profiles are selected in the last 70-95% of the ELM cycle. Compared to the profiles before Ne injection, the most significant change after injection is the dramatic increase in density pedestal top and gradient, especially, the pedestal density gradient $|dn_e/d\psi_N|$ increases by $\sim 90\%$ from 27 to 51. The primary reason for the increases in density pedestal top and gradient is thought to be the improvement of particle confinement as will be discussed in the following. Due to radiation cooling effect and increase in plasma density, the pedestal electron temperature T_e has been reduced. The lower pedestal T_e is compensated by the increase of pedestal n_e resulting in no significant change in the pedestal top pressure,

in agreement with the observation of almost unchanged stored energy. The steeper density gradient leads to a moderate increase of $\sim 28\%$ in pedestal pressure gradient $|dp_{\text{tot}}/d\psi_N|$ (from 70 to 90). In addition, little change is observed in the edge current density estimated from Sauter model [22, 23], which can be a result of the combination of steeper density gradient, reduced electron temperature and higher collisionality. Note that, there is no measurement of effective charge number Z_{eff} in discharge #69033 which is needed in the calculations of total pressure and edge current density. The Z_{eff} is estimated from the similar discharge with the assumption that there is no significant change in Z_{eff} during the ELM transition. The analysis of a similar Ne injection experiment could demonstrate that the change of impurity level is not the key factor responsible for the occurrence of large ELMs in physics in this case. This aspect will be discussed in detail at the end of this section.

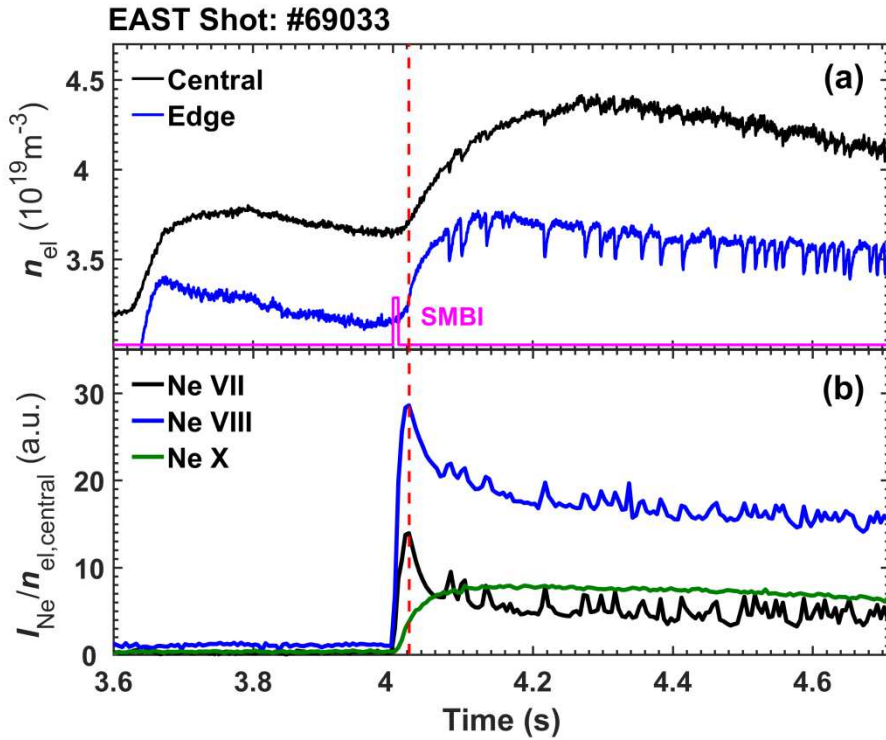


Fig. 3. Time traces for the discharge #69033 of (a) central and edge line-averaged densities, (b) intensities of edge Ne VII, Ne VIII and core Ne X emissions in the main plasma normalized by central line-averaged density.

The reasons responsible for the significant increase in density pedestal top and gradient are firstly discussed here. The contribution of impurity ionization to the increase in electron density could be assessed from Fig. 3, which shows the Ne

emissions in the main plasma measured by extreme ultraviolet (EUV) spectrometer [24] and the core and edge line-averaged densities measured by central (at the midplane $Z = 0$) and outermost ($Z = -42.5$ cm) horizontal chords of POLarimeter-INTerferometer (POINT) diagnostic [25, 26]. Note that the edge line-averaged density $n_{el,edge}$ which covers the range of $\psi_N \sim 0.6-1$ could also exhibit the increase of ELM size. It is found that the temporal evolutions of line-averaged densities are rather inconsistent with the Ne emission evolution. When the edge Ne emission peaks (red line), the plasma density just begins to rise. Then the edge and core Ne emissions soon stay roughly constant, in contrast, the core line-averaged density continues increasing until $t = 4.3$ s. Therefore, we can deduce that impurity ionization is not the primary reason for the increase of plasma density in discharge #69033. It appears that the Ne injection acts as a trigger for the rise of plasma density.

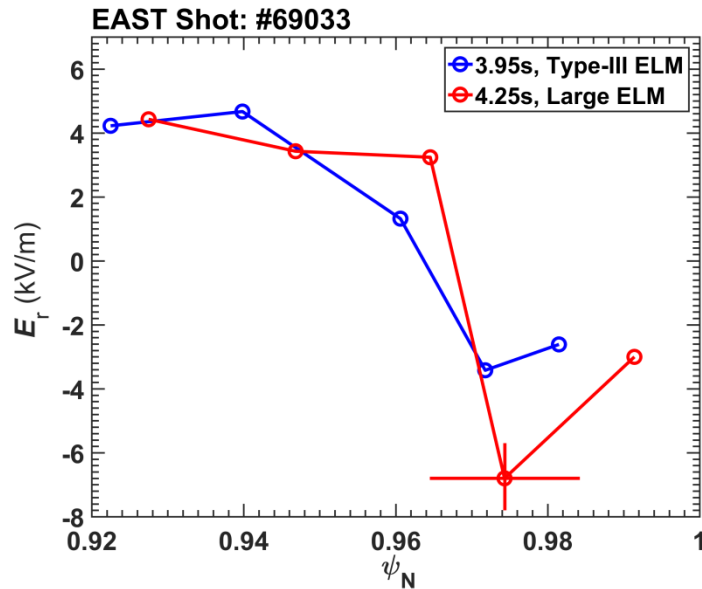


Fig. 4. Radial electric field E_r profiles in the pedestal region at 3.95 s (blue line) and 4.25 s (red line) of discharge #69033.

Particle confinement improvement is thought to be the primary reason responsible for the increase in plasma density. It has been observed from lithium beam emission spectroscopy (Li-BES) diagnostic that the turbulence intensity at the frequency of 40-100 kHz in the pedestal region reduces after Ne injection. However, the Li-BES data quality is not good enough in this shot and thus has not been shown here. Fig. 4 shows the pedestal radial electric field E_r measured by Doppler backscattering system (DBS) diagnostic [27]. It is found that the radial electric field

E_r after Ne injection is more negative and the E_r shear is larger than that before injection. Note that, previous theoretical studies have also indicated that impurity potentially suppresses some turbulence modes, such as ion temperature gradient-driven (ITG) turbulence [28] and trapped electron mode (TEM) [29]. Similar impurity-induced turbulence reduction has also been observed in TEXTOR-94 [30] and DIII-D [31] with Ne injection.

Besides particle confinement improvement and impurity ionization, the reduction of ELM induced particle flux may also help the increase of plasma density. In this work, the ELM amplitude is roughly defined as the height of divertor D_α emission from the baseline to the peak for an ELM burst, i.e. $A_{\text{ELM}} = D_\alpha^{\text{peak}} - D_\alpha^{\text{bottom}}$, which is previously utilized in the ELM studies on JT-60U [32] and EAST [16]. The product of ELM amplitude and frequency $A_{\text{ELM}} \times f_{\text{ELM}}$ is used here as a proxy for the particle flux induced by ELMs. The calculation indicates that the product $A_{\text{ELM}} \times f_{\text{ELM}}$ in the large ELM phase is only ~20% of that in the type-III ELM phase, suggesting that the ELM induced particle flux is reduced with the ELM transition that could help the increase of plasma density.

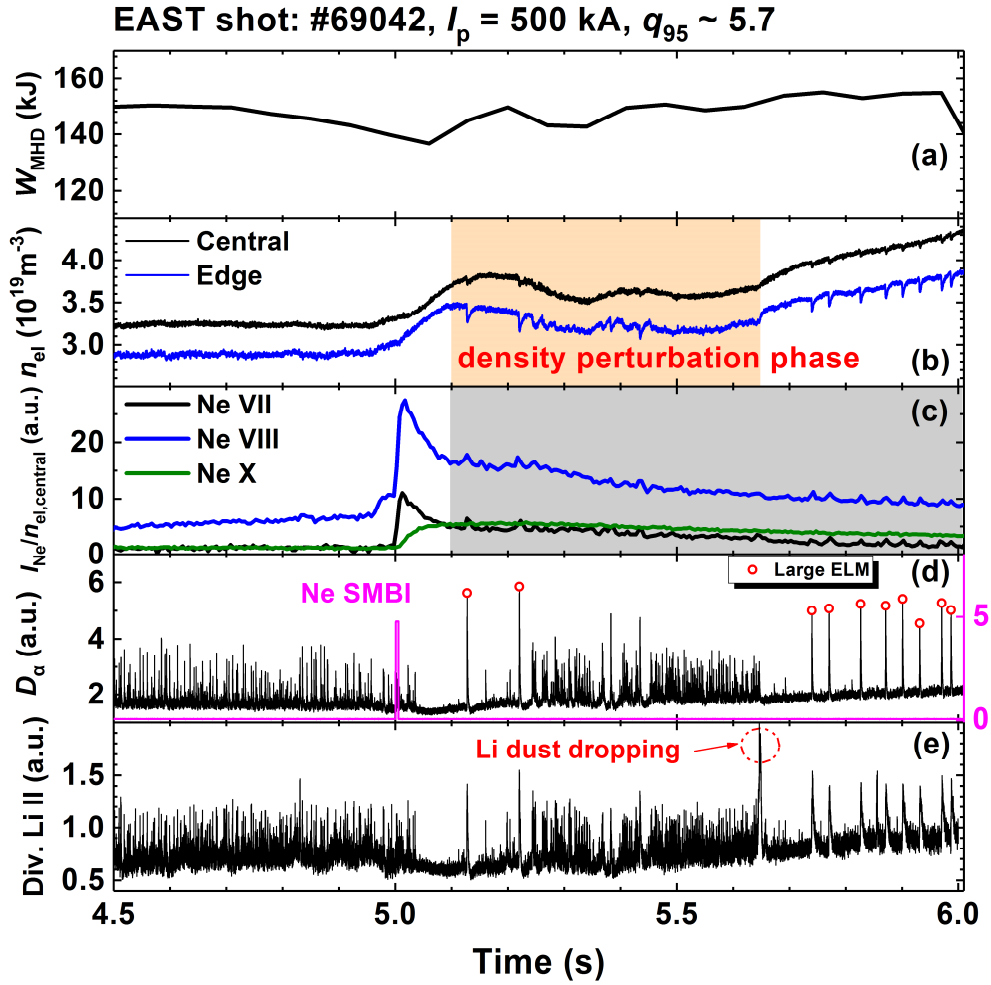


Fig. 5. Time traces for discharge #69042 of (a) stored energy, (b) central and edge line-averaged densities, (c) Ne emissions normalized by $n_{\text{el,central}}$, (d) divertor D_{α} emission and the monitor of SMBI pulse and (e) divertor Li II emission. In this discharge, a pure Ne pulse of 5 ms is injected into plasma by SMBI at $t = 5$ s, and the large ELMs after Ne injection are marked by the red circles.

Another similar Ne injection discharge could provide more insight into the effects of plasma density and impurity level on the ELM behavior, as shown in Fig. 5. The operational parameters of discharge #69042 are similar to that of discharge #69033. Before Ne injection the plasma is also operated in type-III ELMy H-mode plasma. A pure Ne pulse of 5 ms is injected into the plasma by SMBI at $t = 5$ s without degradation of stored energy.

A strong correlation between the occurrence of large ELMs and high edge density can be observed in this discharge as illustrated in Figs. 5(b) and (d). It shows that, after Ne injection the central and edge line-averaged densities increase and a

density perturbation occurs in the period of $t = 5.1\text{-}5.65$ s (orange shadow area). Note that, in this phase the large ELM bursts occur when the edge line-averaged density $n_{\text{el,edge}}$ (covering the range of $\psi_N \sim 0.6\text{-}1$) is relatively higher, and the small type-III ELMs recover when the $n_{\text{el,edge}}$ is relatively lower. Particularly, after $t = 5.65$ s, the plasma density increases continuously, meanwhile the type-III ELMs completely disappear and are replaced by the low-frequency large ELMs. The reason for the continuous increase in plasma density after $t = 5.65$ s may be associated with the sudden dropping of lithium dust as illustrated in Fig. 5(e). This shot further demonstrates that occurrence of large ELMs is highly correlated with the edge density. Unfortunately, a reliable measurement of edge density profile is not available in this discharge.

It is worth noting that, this experiment also reveals that the impurity level is not the primary reason for the triggering of large ELMs in physics. As shown in Fig. 5(c), the temporal evolutions of Ne emissions in discharge #69042 are similar to that in discharge #69033, qualitatively reflecting the evolution of impurity level in the main plasma. It shows that both large ELMs and small type-III ELMs can occur while the Ne emissions remain roughly constant after $t = 5.1$ s (grey shadow area), implying that impurity injection just acts as a switch-on of the ELM transition but the impurity level is not the key factor for the occurrence of large ELMs in physics in our case.

The Ne concentration in discharge #69033 has been roughly estimated. It is known that the first ionization energies of deuterium and Ne particles are relatively low and close, i.e. 13.6 eV for deuterium and 21.6 eV for Ne. The SMBI fuelling efficiency of deuterium (D_2) gas under H-mode plasma is found to be 6%-12% in EAST [33]. Therefore, with a reasonable assumption of ~12% fuelling efficiency for SMBI Ne gas, the volume-averaged Ne concentration is estimated to be on the order of ~1% of electron density in the early phase of Ne injection and ~0.6% for the stationary large ELM phase.

3. Exploration of underlying mechanism for the transition to large ELMs with numerical simulation

Currently the peeling-ballooning theory [34, 35] is generally considered to explain the onset of large ELMs. Based on the theory, the kink/peeling modes and ballooning modes can couple to peeling-ballooning modes (PBMs) that trigger a large ELM with high pedestal pressure gradient and high edge current density. In this section, in order to explore the underlying mechanism for the transition to large ELMs

with Ne injection, linear PB stability analysis with the ideal MHD eigenvalue ELITE code [36] and the initial-value NIMROD code [37] and nonlinear simulation of ELM crash with the initial-value BOUT++ code [38] are carried out. In addition, a scan of pedestal density gradient in the linear stability analysis is performed to further study the role of density gradient on pedestal stability and the ELM transition.

The experimental equilibria of discharge #69033 for simulation are generated with kinetic EFIT code [39] within the constraints of the measured profiles. Considering that the edge ion temperature T_i and electron temperature T_e in EAST are relatively low and the edge collisionality is high, the assumption $T_i = T_e$ in the edge region is made as the plasma at high edge collisionality has a good energy equipartition between ions and electrons. A uniform Z_{eff} profile of the measured averaged Z_{eff} value is assumed in the EFIT equilibrium reconstruction. Since the Z_{eff} has not been measured in discharge #69033, the accurate variation of Z_{eff} is unknown. Nevertheless, as discussed in section 2, the Ne concentration is roughly estimated to be relatively low, and the change of impurity level is not the key factor accounting for the occurrence of large ELMs in physics mechanism in our case. Therefore, in this section the influence of Z_{eff} variation on PB instabilities is ignored in the stability analysis and the Z_{eff} is set equal to the similar discharge value of $Z_{\text{eff}} = 2$. The effect of Z_{eff} variation on pedestal stability will be further discussed in section 4.1.

3.1. Linear stability analysis with ELITE and NIMROD codes

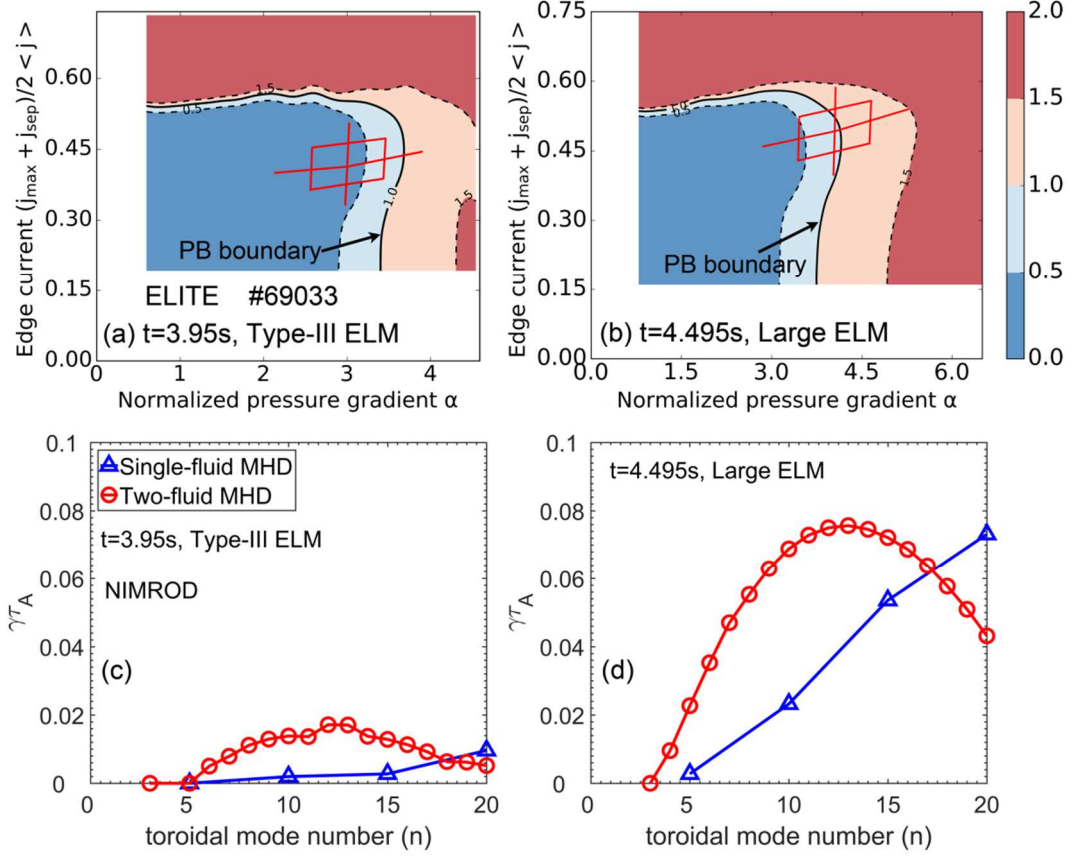


Fig. 6. Operational points and PB stability boundaries calculated by ELITE code and normalized growth rates of PBMs computed by NIMROD code in single-fluid MHD (blue) and two-fluid MHD (red) models for (a) (c) type-III ELMs and (b) (d) large ELMs of discharge #69033. The stability boundary is defined as the value when $\gamma/(\omega_{*i}/2)$ is equal to 1.

Figs. 6(a) and (b) show the operational points and PB stability boundaries calculated with ELITE code for type-III ELM and large ELM phases of discharge #69033, in terms of the normalized edge current density and normalized pedestal pressure gradient ($\alpha = -\frac{2V'}{(2\pi)^2} \left(\frac{V}{2\pi^2 R}\right)^{\frac{1}{2}} \mu_0 p'$, where V is the plasma volume enclosed by the flux surface, p is the pressure, and the prime represents the derivative with respect to the poloidal flux ψ). The stability boundary is defined as the value when $\gamma/(\omega_{*i}/2)$ is equal to 1, where γ is the growth rate of the most unstable mode and ω_{*i} is the ion diamagnetic frequency. It shows that the operational point for large ELM case is located more close to the PB boundary than that for type-III ELM case. Consistently, the NIMROD result shown in Figs 6(c) and (d) shows that the growth rates of $n = 3-20$ modes for type-III ELM case are very low for both single-fluid and

two-fluid models, whereas the large ELM case is significantly more unstable with much higher growth rates.

It is worth pointing out that the linear NIMROD results of single-fluid and two-fluid MHD models are quite different. In contrast to the single-fluid model, the non-ideal effects such as finite-Larmor-radius (FLR) effect, two-fluid Hall and electron diamagnetic drift are included in the two-fluid model. In the NIMROD results, the growth rates of high- n modes are reduced in two-fluid model due to the well-known ion diamagnetic stabilization [40-42]. More significantly, the growth rates of low- n and intermediate- n PBMs computed with two-fluid model are remarkably higher than that computed with single-fluid model, suggesting that the two-fluid effects can significantly destabilize the low- n and intermediate- n PB instabilities. Further analysis in section 3.3 will indicate that this destabilization of low- n and intermediate- n PB instabilities from two-fluid effects is correlated with the pedestal density gradient, which could contribute to the triggering of large ELMs.

3.2. Nonlinear simulation of ELM crash with BOUT++ code

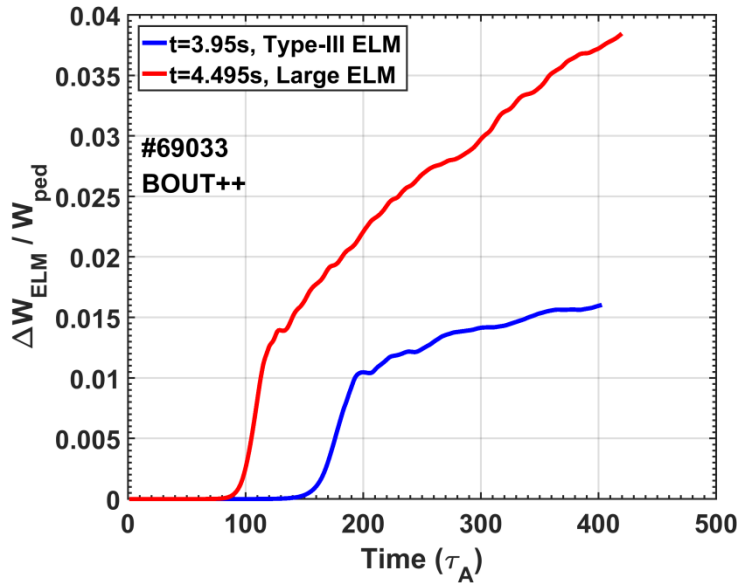


Fig. 7. Time history of the ELM energy loss fraction ($\Delta W_{ELM}/W_{ped}$) for type-III ELM case (blue) and large ELM case (red) in the nonlinear BOUT++ simulation, τ_A is the Alfvén time.

The above linear analysis has indicated that the large ELM case is more unstable than the other with respect to PB instabilities. Furthermore, nonlinear simulation of ELM crash for type-III ELM and large ELM of discharge #69033 has also been

conducted with the BOUT++ five-field two-fluid model in this paper. The BOUT++ code is an initial-value MHD code with non-ideal physics effects, including ion diamagnetic drift, $E \times B$ drift, resistivity, hyper-resistivity, etc. Over the last decade, BOUT++ code has been successfully applied to simulate the nonlinear ELM collapse [38, 43].

Fig. 7 shows the simulated time evolution of ELM energy loss fraction for type-III ELM and large ELM cases. The ELM energy loss fraction is defined as the ratio of ELM energy loss ΔW_{ELM} to the pedestal stored energy W_{ped} ,

$$\frac{\Delta W_{\text{ELM}}}{W_{\text{ped}}} = \frac{\langle \int_{\psi_{\text{in}}}^{\psi_{\text{out}}} d\psi \phi J d\theta d\zeta (P_0 - \langle P \rangle_{\zeta}) \rangle_t}{\int_{\psi_{\text{in}}}^{\psi_{\text{out}}} P_0 d\psi \phi J d\theta d\zeta}, \quad (1)$$

where P_0 is the pre-ELM pressure, P is the pressure during the ELM collapse, $\langle \rangle_{\zeta}$ is the average over the bi-normal periodic coordinate, the lower integral limit is the pedestal inner radial boundary ψ_{in} , while the upper limit is the radial position of the peak pressure gradient ψ_{out} , J is the Jacobian. The simulated ELM amplitude ratio of large ELM to type-III ELM is in good agreement with the experimental observation. At the simulation time $t = 400 \tau_A$, the ratio of the ELM energy loss fraction of large ELM to that of type-III ELM is about 2.3. In the discharge #69033, the averaged amplitude of divertor D_{α} emission burst of large ELMs is about 1.9 times as large as that of type-III ELMs.

3.3. Direct destabilizing effect of pedestal density gradient on low- n and intermediate- n PBMs

With the above analysis, the physical reason for the impurity-induced transition to large ELMs is not yet fully clear. The impurity effects, including dilution effect, increased Z_{eff} and lower separatrix temperature $T_{\text{e,sep}}$, are usually considered. The impurity can reduce the main ion density through dilution effect, which may have a stabilizing effect on the pedestal instabilities [15]. Increased Z_{eff} can reduce the edge bootstrap current or provide a stabilizing effect through higher resistivity [44]. In addition, lower $T_{\text{e,sep}}$ due to impurity injection could cause an inward shift of pedestal profile that facilitates the stability improvement [15]. Therefore, these impurity effects are beneficial for the pedestal stability, which may be the reasons for the short-lived ELM suppression just after Ne injection but could not contribute to the triggering of large ELMs.

The increase of pedestal density gradient could probably be the key factor for the impurity-induced transition to large ELMs. As suggested from discharge #69042 in

Fig. 5, the occurrence of large ELMs is highly correlated with the edge density. In discharge #69033, the most remarkable change in pedestal profiles after Ne injection is the dramatic increase of pedestal density gradient. In addition, as will be discussed in section 4, more experiments have indicated that the ELM amplitude demonstrates to be strongly correlated with the pedestal density gradient. The conventional understanding is that, the density gradient can affect the pedestal stability through the modifications of pressure gradient and edge current density or ion diamagnetic stabilization effect. However, in discharge #69033 the pedestal pressure gradient only moderately increases and the edge bootstrap current shows minimal change. In addition, the ion diamagnetic frequencies are similar for type-III ELMs and large ELMs, which suggests that the ion diamagnetic stabilization is not the key factor. Therefore, besides the conventional mechanism that steeper pedestal density gradient enhances the pressure gradient and thus destabilizes the PBMs, there might be other density-gradient-related mechanism that could also contribute to the triggering of large ELMs.

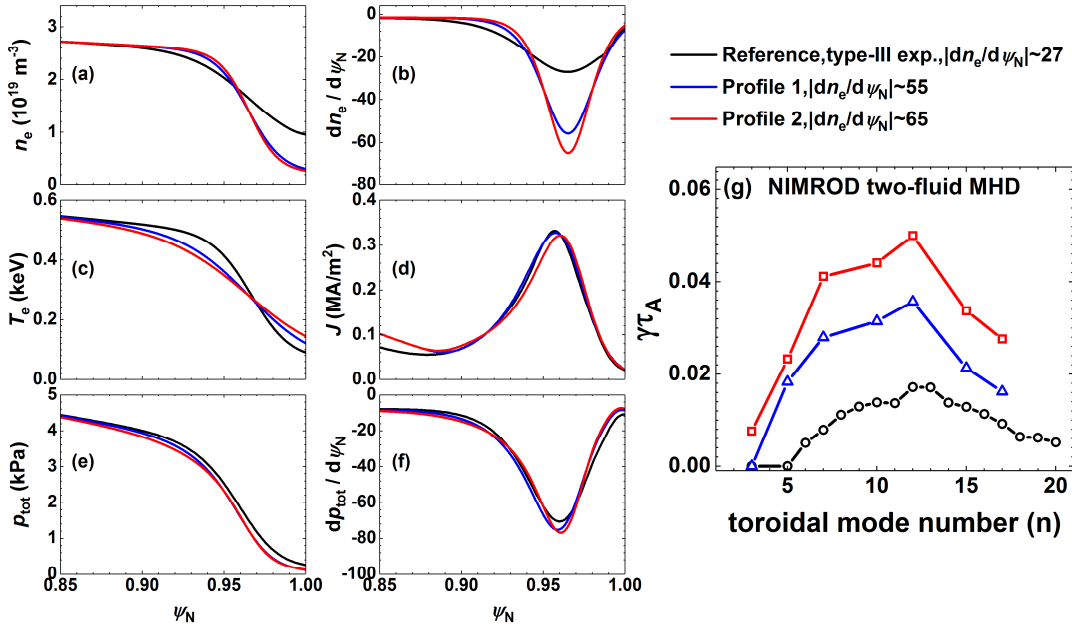


Fig. 8. Scan of pedestal density gradient in the linear NIMROD simulation. Edge profiles of (a) electron density n_e , (b) density gradient $dn_e/d\psi_N$, (c) electron temperature T_e , (d) current density, (e) total pressure p_{tot} and (f) pressure gradient $dp_{\text{tot}}/d\psi_N$; (g) normalized growth rates of PBMs computed with NIMROD two-fluid model. The experimental type-III ELM equilibrium with $|dn_e/d\psi_N| \sim 27$ is taken as the reference case. The pedestal densities and temperatures of profile 1 ($|dn_e/d\psi_N| \sim 55$) and profile 2 ($|dn_e/d\psi_N| \sim 65$) cases are artificially constructed with the modified tanh

function, while keeping the peak pressure gradient and peak edge current density almost unchanged.

In order to further explore the role of pedestal density gradient on PB instabilities and the ELM transition in discharge #69033, in the following we keep the peak pressure gradient $|dp_{\text{tot}}/d\psi_N|$ and peak edge current density almost unchanged and scan the pedestal density gradient $|dn_e/d\psi_N|$ in the linear NIMROD calculation. As shown in Fig. 8, the experimental type-III ELM equilibrium with $|dn_e/d\psi_N| \sim 27$ is taken as the reference case in the scan of $|dn_e/d\psi_N|$. The pedestal densities and temperatures of the cases profile 1 with $|dn_e/d\psi_N| \sim 55$ and profile 2 with $|dn_e/d\psi_N| \sim 65$ are artificially constructed with the modified tanh function and the positions of peak gradients of density and temperature are fixed. The density and temperature profiles in the plasma core are kept unchanged and the Z_{eff} value is same for these cases. In the scan of $|dn_e/d\psi_N|$, we increase the pedestal density gradient, reduce the pedestal temperature gradient and slightly adjust the collisionality simultaneously to keep the peak values of recalculated $|dp_{\text{tot}}/d\psi_N|$ and edge current density almost unchanged (the variations of peak $|dp_{\text{tot}}/d\psi_N|$ and edge current density are less than 10%). As input to NIMROD calculation, the new equilibria are reproduced by using the toroidal equilibrium module (TEQ) in the CORSICA code [45] within the constraints of constructed profiles.

The NIMROD two-fluid calculation result in Fig. 8(g) shows that the growth rates of PBMs increase with $|dn_e/d\psi_N|$ though the pressure gradient and edge current density are almost unchanged. We note that the value of constructed density near the separatrix is very low that may affect the simulation result through ion diamagnetic stabilization [46]. Therefore, the density near the separatrix is artificially modified while the electron temperatures are unchanged, as termed as the profile 3 and profile 4 cases in Fig. 9. With the new reconstructed equilibria, linear stability analysis using both single-fluid (dash line) and two-fluid MHD (solid line) models has been performed as illustrated in Fig. 9(g). It is found that the growth rates of low- n and intermediate- n PBMs significantly increase with $|dn_e/d\psi_N|$ in the two-fluid calculation. This result demonstrates that the pedestal density gradient could directly destabilize the low- n and intermediate- n PBMs, independent of the changes of pressure gradient and current density, which could contribute to the triggering of large ELMs.

It is worth mentioning that this destabilizing effect of density gradient is evident only in the two-fluid MHD simulation. For the single-fluid MHD model without

two-fluid effects, in contrast, the PB instabilities in the three cases are almost stable with very low growth rates. This result is reasonable since the pressure gradient and current density, which act as ballooning drive and peeling drive, are relatively low in the single-fluid model. The difference between single-fluid and two-fluid calculation results suggests that the direct destabilizing effect of density gradient on low- n and intermediate- n PBMs derives from the two-fluid effects.

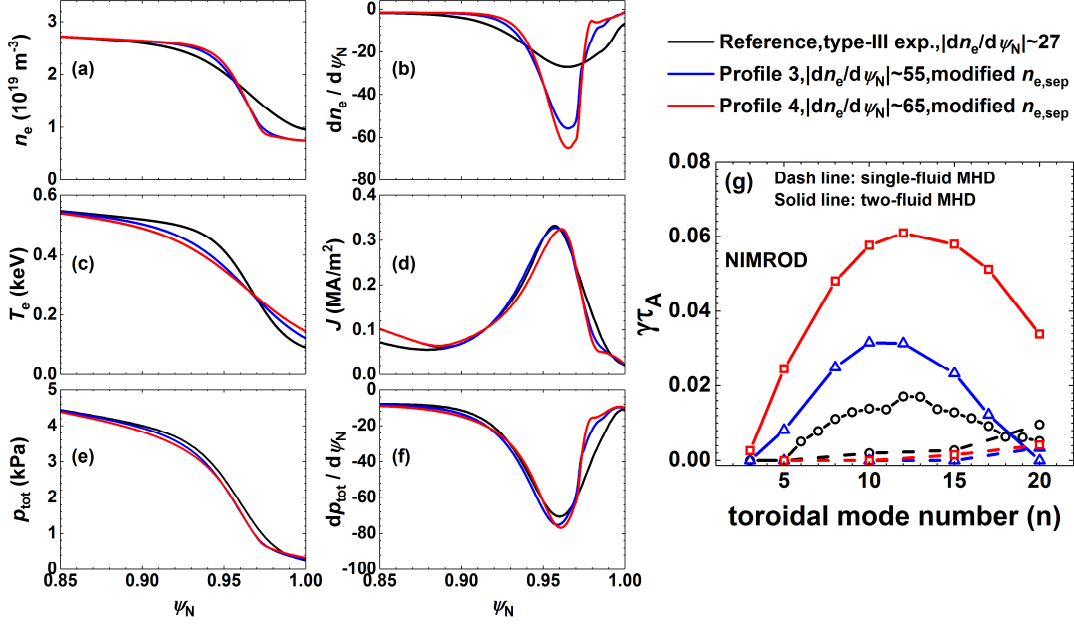


Fig. 9. Scan of pedestal density gradient with modified separatrix density in the linear NIMROD simulation. Edge profiles of (a) electron density n_e , (b) density gradient $dn_e/d\psi_N$, (c) electron temperature T_e , (d) current density, (e) total pressure p_{tot} and (f) pressure gradient $dp_{\text{tot}}/d\psi_N$; (g) normalized growth rates of PBMs computed with NIMROD single-fluid (dash line) and two-fluid (solid line) models. The temperature profiles and peak density gradients of the profile 3 and profile 4 cases are the same as that in the profile 1 and profile 2 cases in Fig. 8.

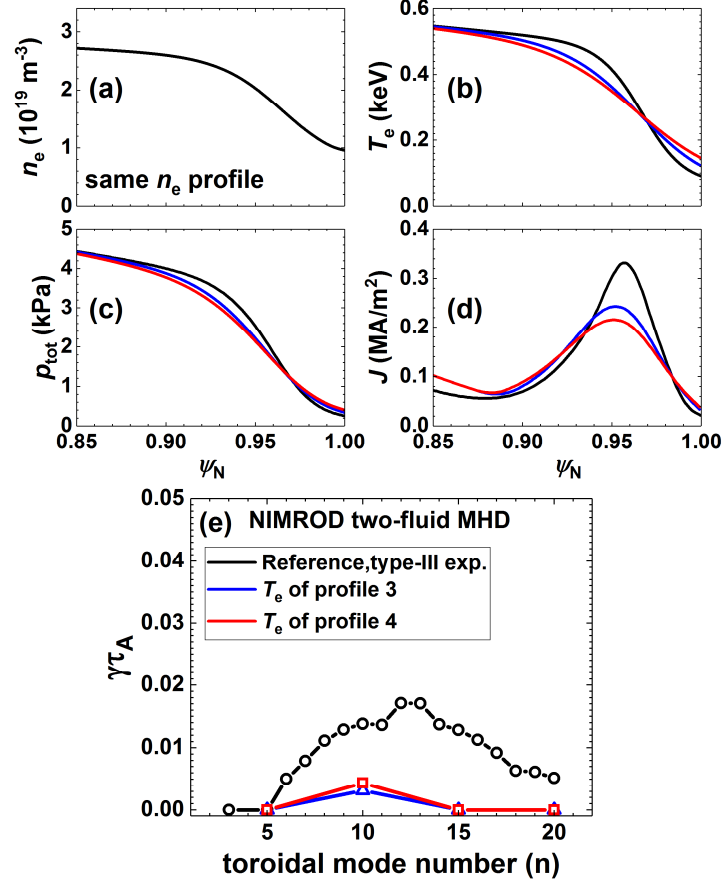


Fig. 10. Examining of the influence of pedestal temperature variation on the density gradient scan simulation result in Fig. 9. Edge profiles of (a) electron density n_e , (b) electron temperature T_e , (c) total pressure p_{tot} and (d) current density; (e) normalized growth rates of PBMs in the two-fluid calculation. The density profile is from experimental type-III ELM equilibrium and fixed, the T_e profiles are the same as those in Fig. 9(c).

In the scan of density gradient in Fig. 9, the pedestal electron temperature T_e has also changed. Therefore it is needed to examine the influence of temperature variation on the simulation result of density gradient scan. As shown in Fig. 10, the edge density profile is fixed as the n_e of experimental type-III ELM equilibrium, and the T_e profiles are the same as those in Fig. 9(c). The result shows that, with the reduction of T_e gradient, both pressure gradient and current density decrease and the PBMs become more stable. This suggests that, the increase of peeling-ballooning growth rates is not contributed from the pedestal temperature variation in the simulation of density gradient scan in Fig. 9.

Numerical simulation of density (i.e. collisionality) scan has also been performed in reference [47] to explain the collisionality scaling of type-I ELM energy loss. In

their density scan simulation, pressure profile is fixed with different partitions between density and temperature profiles, and thus the edge current density decreases with increasing density (i.e. collisionality). Their study suggests that the pedestal density plays a role in PB instabilities and ELM amplitude through its effect on edge current density and ion diamagnetic stabilization, and as a result the ELM energy loss decreases with increasing density (i.e. collisionality). Different to their simulation, our experimental observation in discharge #69033 indicates that the ELM amplitude increases with higher plasma density. In our simulation, we focus on the pedestal density gradient and scan it while keeping the pressure gradient and edge current density almost unchanged. Our simulation indicates that, the direct destabilizing effect of density gradient on low-n and intermediate-n PB instabilities via two-fluid effects could also play an important role in the triggering of large ELMs with impurity injection.

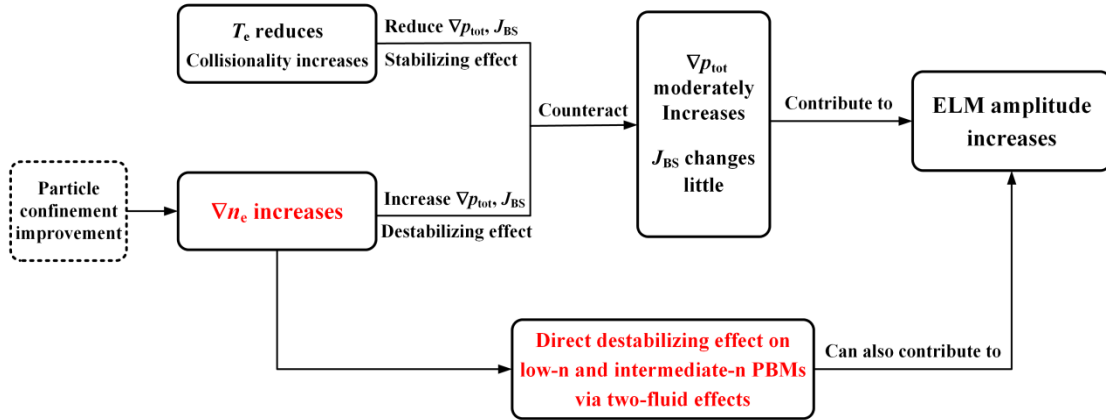


Fig. 11. Flowcharts showing the underlying mechanism of the transition to large ELMs in discharge #69033.

Overall speaking, the underlying mechanism for the impurity-induced transition to large ELMs is illustrated in Fig. 11. With Ne injection, the pedestal temperature decreases and thus edge collisionality increases, which can reduce the pressure gradient and edge bootstrap current. Significantly, the pedestal density gradient shows a remarkable increase potentially due to the reduction of edge turbulence transport. On the one hand, the increase in pedestal density gradient can counteract the roles of lower temperature and higher edge collisionality, and consequently the pressure gradient only moderately increases and edge bootstrap current shows minimal change. This moderate increase in pressure gradient could destabilize the high-n ballooning modes. On the other hand, the steeper pedestal density gradient can directly

destabilize the low- n and intermediate- n PB instabilities via two-fluid effects, independent of the modifications of pressure gradient and edge current density, which could also contribute to the triggering of large ELMs. Therefore the pedestal density gradient seems to play a critical role in the transition to large ELMs with Ne injection.

The effect of pedestal density gradient on ELM amplitude still remains two open questions. One is the physics behind the two-fluid effects through which density gradient affects the linear PB instabilities. Further analysis of this two-fluid effects requires a complex modification of current MHD codes, and the physics behind it should be further studied with the development of NIMROD code or other MHD codes in the future. Moreover, the ELM amplitude is determined by the nonlinear ELM collapse process, the role of density gradient in the nonlinear process is the other open question that requires more deeper physical understanding in the future work.

4. Discussion

4.1. Effect of Z_{eff} variation on the pedestal stability

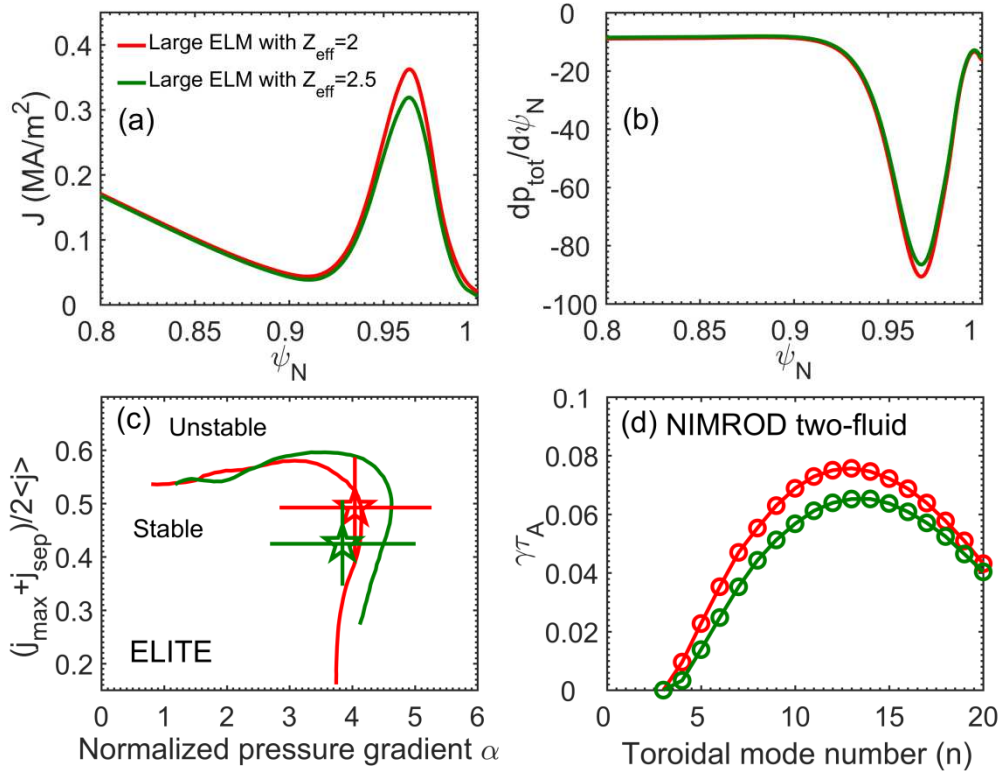


Fig. 12. Edge profiles of (a) current density and (b) pressure gradient, (c) pedestal stability diagrams calculated by ELITE code and (d) normalized growth rates of

PBMs calculated by NIMROD code for large ELM case with $Z_{\text{eff}} = 2$ (red) and $Z_{\text{eff}} = 2.5$ (green).

We have estimated the increase of Z_{eff} and its effect on the stability analysis taking a plausible Ne concentration. We assume that: 1) the dominant impurities in the main plasma are intrinsic carbon (C) and extrinsic Ne, and both impurity species are fully ionized; 2) the C concentration is nearly constant when Ne is injected. As estimated in the last paragraph of section 2, the Ne concentration is $\sim 0.6\%$ of electron density in the large ELM phase. From the definition of Z_{eff} (i.e. $Z_{\text{eff}} = \sum_j n_j Z_j^2 / n_e$) and charge conservation (i.e. $n_e = \sum_j n_j Z_j$), it can be estimated that the Z_{eff} value increases from $Z_{\text{eff}} = 2$ to $Z_{\text{eff}} = 2.5$ after Ne injection.

The effect of Z_{eff} variation on the edge bootstrap current and peeling-ballooning instability is illustrated in Fig. 12. It shows that the increased Z_{eff} can reduce the edge current density and thus has a stabilizing effect on the PB instabilities. This result suggests that the change of Z_{eff} is not the reason for the transition to large ELMs.

4.2. Correlation between ELM amplitude and pedestal density gradient

In addition to the experiments described in this paper, substantial experimental studies in the past decade have also demonstrated that the ELM amplitude is highly correlated with the pedestal density gradient. The EAST study [48] of grassy ELM regime has pointed out that the grassy ELMy H-mode is characterized by a wide pedestal with a low density gradient and a high density ratio $n_{e,\text{sep}}/n_{e,\text{ped}}$ between the pedestal foot and top in contrast to the large-amplitude type-I ELMs, which plays an important role in the access to such small ELM regime. In the favorable B_t configuration, i.e. the ion ∇B drift towards the primary X-point, such grassy ELMs with low pedestal density gradient and type-I ELMs with high density gradient are also observed on EAST, as illustrated in figure 17 of reference [49]. In DIII-D, small grassy ELM regime has also been achieved with the assistance of resonant magnetic perturbation (RMP) [50] or naturally obtained in the operational space of high heating power, high q_{95} and high β_p [51]. Studies indicate that both RMP-assisted and intrinsic grassy ELM regimes in DIII-D have a flat and wide density pedestal with low gradient in contrast to large ELMs, consistent with the experimental results in EAST. Besides, the ELM-free regime, achieved in NSTX with increasing lithium wall

coating, also demonstrates a strong correlation between ELM suppression and pedestal density width (i.e. density gradient) [52, 53].

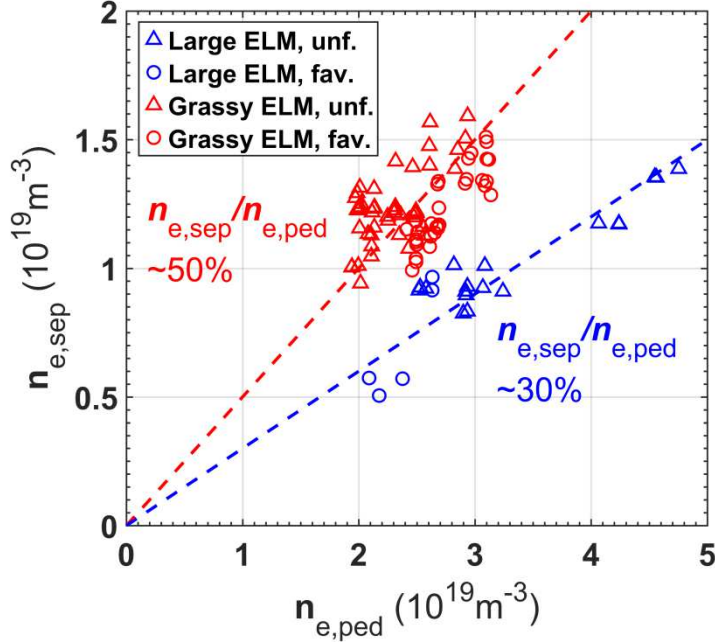


Fig. 13. Diagram of separatrix electron density $n_{e,sep}$ vs. pedestal electron density $n_{e,ped}$ for natural grassy ELM and large ELM discharges under favorable and unfavorable B_t in EAST.

A statistical result of pedestal density gradient of EAST natural grassy ELM and large ELM discharges under favorable and unfavorable B_t is shown in Fig. 13. Here the large ELM is defined as the fluctuation of edge line-averaged density $n_{el,edge}$ due to ELMs larger than 4%, while the $n_{el,edge}$ fluctuation of small grassy ELMs is less than 0.3%. The ratio of separatrix electron density $n_{e,sep}$ to pedestal electron density $n_{e,ped}$ is taken as a proxy for pedestal density gradient, i.e. a higher density ratio $n_{e,sep}/n_{e,ped}$ represents a lower density gradient. It shows that the grassy ELMs are characterized by a high density ratio $n_{e,sep}/n_{e,ped} \sim 50\%$ while $n_{e,sep}/n_{e,ped} \sim 30\%$ for large ELMs. This demonstrates that the pedestal density gradient of large ELM discharge is systematically steeper than that of small grassy ELM discharge regardless of whether the plasma is operated in favorable B_t or unfavorable B_t . The typical density profiles of grassy ELM and large ELM discharges under favorable B_t are illustrated in Fig. 14. It shows that the pedestal density profile is relatively flat in the grassy ELM discharge while more steeper for large ELM discharge regardless of the divertor configuration. These results indicate that the correlation between ELM amplitude and pedestal density gradient could be widely observed in EAST experiments.

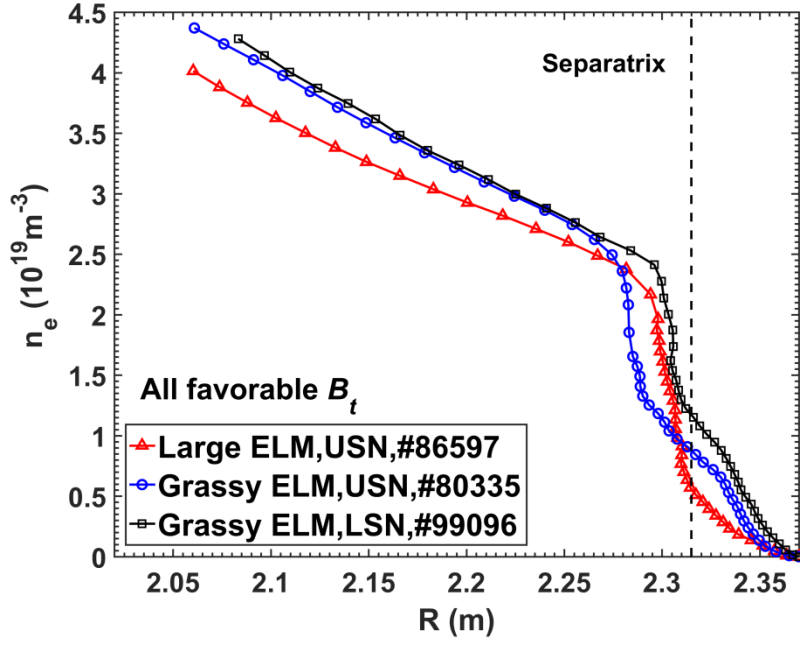


Fig. 14. Density profiles of EAST grassy ELM and large ELM discharges under favorable B_t .

Overall speaking, substantial experiments on multiple tokamak devices have demonstrated that ELM amplitude is strongly related to the pedestal density gradient. Large-amplitude ELMs generally occur with a steep density gradient in the pedestal, while the achievement of small-amplitude ELM regime relies on a flat density pedestal with low gradient. The physics behind the strong correlation between ELM amplitude and pedestal density gradient may be the two aspects as pointed out in section 3.3. On the one hand, density gradient can modify the pressure gradient and edge bootstrap current. On the other hand, a steep density gradient can provide a direct destabilizing effect on low- n and intermediate- n PBMs via two-fluid effects.

5. Summary and future plan

An anomalous transition from type-III to large ELMs induced by Ne injection at overlapping q_{95} space between large and small ELMs has been observed in EAST. In the pedestal region, the electron temperature decreases and thus the collisionality increases after Ne injection. Potentially due to the reduction of edge turbulence transport, the pedestal density gradient shows a remarkable increase. As a result, the pressure pedestal gradient increases moderately and edge current density has minimal change. A similar experiment further demonstrates that the occurrence of large ELMs after Ne injection is highly correlated with the edge density. Linear PB stability

analysis indicates that the large ELM case is more unstable than the type-III ELM case during the ELM transition. Nonlinear simulation has successfully reproduced the ELM crash processes of type-III and large ELMs, and the simulated ELM amplitude ratio of large ELM to type-III ELM is in good agreement with the experimental observation. The effect of Z_{eff} variation on pedestal stability has been examined, and the result shows that the increase of Z_{eff} has a stabilizing effect on the PB instabilities suggesting the change of Z_{eff} is not the key factor for the ELM transition. In order to further study the role of pedestal density gradient itself on the ELM transition, a scan of pedestal density gradient in linear stability analysis has been performed while keeping the peak values of pressure gradient and edge current density almost unchanged. The result reveals that, besides the effect of moderate increase in pressure gradient, the direct destabilizing effect of steep pedestal density gradient on low- n and intermediate- n PB instabilities via two-fluid effects could also facilitate the transition to large ELMs in this impurity injection experiment.

Substantial experiments on multiple tokamak devices have demonstrated that the ELM amplitude is strongly correlated with the pedestal density gradient. Based on the analysis in this work, there are two underlying mechanisms through which density gradient plays a significant role in the ELM amplitude. On the one hand, pedestal density gradient can affect the pedestal stability and ELM amplitude through the modifications of pedestal pressure gradient and edge current density. On the other hand, a steep density gradient can provide a direct destabilizing effect on low- n and intermediate- n PBMs via two-fluid effects, which may facilitate the triggering of large ELM bursts even at relatively low pressure gradient and low current density. This study could provide more insight into the effect of pedestal density gradient on pedestal stability and ELM behavior, and thus help the control of large-amplitude ELMs.

Similarly, it has also been observed in JET-ILW that the ELM energy loss increases with impurity seeding [11]. The background plasmas in JET-ILW are operated in type-I ELMy H-mode with high NBI heating power, and the nitrogen (N_2) gas is seeded into the plasma. With N_2 seeding, the pedestal density and temperature increase and the confinement in JET-ILW recovers to the level comparable to JET-C, accompanied by the increase of ELM energy loss. In contrast, the background plasma in EAST discharge is type-III ELMy H-mode under relatively low heating power. The increase of pedestal density is also observed in EAST, however the most significant change in pedestal profiles is the dramatic increase of density gradient. The reason for

the larger ELM size in JET-ILW may be that the nitrogen-seeded operational point with higher pressure gradient and edge current density lies in the unstable region with respect to the PB boundary while the operational point without seeding lies in the stable region [54]. Our finding indicates that the increased ballooning drive due to higher pressure gradient and the direct destabilizing effect of density gradient on low- n and intermediate- n PBMs via two-fluid effects are the two underlying mechanisms for the impurity-induced transition to large ELMs in EAST.

Impurity injection experiments by using SMBI have also been performed in HL-2A with Ne+D₂ gas mixture of different impurity ratios [12]. The responses of ELM behavior to Ne ratios are rather different. 10% Ne injection leads to ELM mitigation, and 30% Ne mixture causes that large ELMs are suppressed and replaced by small-amplitude high frequency bursts. For pure Ne pulse, reduction of ELM frequency has been observed but without significant change in ELM amplitude, partly different from the experimental observation in EAST. In the future, Dedicated impurity injection experiments with different impurity ratios but similar operational parameters are worth being carried out to study the effect of impurity ratio on the ELM response to impurity injection on EAST.

The impact of edge density on ELM behavior has also been studied in ASDEX-Upgrade [55]. Different from the issue of pedestal density gradient effect on ELM behavior in this work, ASDEX-Upgrade experiments address the importance of separatrix density on the ELM size by using different particle fuelling scenarios. At similar plasma profiles inside the separatrix, a high separatrix density leads to small ELMs, whereas large ELMs appear with the reduction of separatrix density. In contrast, the EAST result shows that the separatrix density of large ELMs is somewhat higher than that of type-III ELMs, suggesting that the separatrix density does not play the dominant role in our case.

In this work, it is worth noting that we just consider the profiles in pre-ELM phase during the stability analysis. It would be helpful for the understanding of ELM frequency and amplitude to consider the evolutions of pedestal profile and stability throughout the whole ELM cycle. However, due to the diagnostic constraint, currently the plasma profile in a whole ELM cycle is not yet available. This topic could be further discussed with high-time-resolution Thomson Scattering measurement in the future.

Notably, the commissioning of divertor power load control scheme with radiative divertor technique is planned to be performed in the ITER first pre-fusion power

operation (PFPO-1) phase when the heating power is relatively low [56]. Our study indicates that extrinsic impurity injection may improve the particle confinement and thus increase the pedestal density gradient, which could facilitate the triggering of large ELMs even at relatively low pressure gradient and low current density. Therefore, more attention should be given to the potential risk of impurity-induced large ELMs in the development of radiative divertor regime during the ITER PFPO-1 phase.

Acknowledgements

The authors wish to acknowledge Professors X.L. Zou, T.Y. Xia and G.Q. Li and Doctors P.J. Sun and H. Li for useful discussion. This work was supported by National MCF Energy R&D Program under Grant No. 2019YFE03030000, National Natural Science Foundation of China under Contracts Nos. 12005257, 11922513, 11905143, 12005263, 11975275, Special Research Assistant Funding of CAS, China Postdoctoral Science Foundation under contract No. 2020M671913, CASHIPS Director's Fund, Grant No. YZJJ2020QN13, Key Research Program of Frontier Sciences, CAS, Grant No. QYZDB-SSWSLH001, the Fundamental Research Funds for the Central Universities at Huazhong University of Science and Technology Grant No. 2019kfyXJJS193, the National Magnetic Confinement Fusion Program of China Grant No. 2019YFE03050004 and the US Department of Energy Grant Nos. DE-FG02-86ER53218 and DE-SC0018001. This research used the computing resources from the Supercomputing Center of University of Science and Technology of China. We are grateful for support from the NIMROD team.

References

- [1] E.J. Doyle, W.A. Houlberg, Y. Kamada, et al., *Nucl. Fusion* 47 (2007) S18.
- [2] Y.X. Wan, J.G. Li, Y. Liu, et al., *Nucl. Fusion* 57 (2017) 102009.
- [3] Y. Liang, *Fusion Sci. Technol.* 59 (2017) 586.
- [4] M.N.A. Beurskens, G. Arnoux, A.S. Brezinsek, et al., *Nucl. Fusion* 48 (2008) 095004.
- [5] N. Asakura, T. Nakano, N. Oyama, et al., *Nucl. Fusion* 49 (2009) 115010.
- [6] P.A. Schneider, E. Wolfrum, M.G. Dunne, et al., *Plasma Phys. Control. Fusion* 56 (2014) 025011.
- [7] T.H. Osborne, G.L. Jackson, Z. Yan, et al., *Nucl. Fusion* 55 (2015) 063018.

- [8] R. Maingi, T.H. Osborne, B.P. Leblanc, et al., *Phys. Rev. Lett.* 103 (2009) 075001.
- [9] J.S. Hu, Z. Sun, H.Y. Guo, et al., *Phys. Rev. Lett.* 114 (2015) 055001.
- [10] R. Maingi, J.S. Hu, Z. Sun, et al., *Nucl. Fusion* 58 (2018) 024003.
- [11] L. Frassinetti, D. Dodt, M.N.A. Beurskens, et al., *Nucl. Fusion* 55 (2015) 023007.
- [12] W.L. Zhong, X.L. Zou, B.B. Feng, et al., *Nucl. Fusion* 59 (2019) 076033.
- [13] K. Wu, Q.P. Yuan, B.J. Xiao, et al., *Nucl. Fusion* 58 (2018) 056019.
- [14] X.W. Zheng, J. Li, J. Hu, et al., *Plasma Phys. Control. Fusion* 55 (2013) 115010.
- [15] S. Saarelma, A. Järvinen, M. Beurskens, et al., *Phys. Plasmas* 22 (2015) 056115.
- [16] Q.Q. Yang, G.S. Xu, N. Yan, et al., *Nucl. Fusion* 60 (2020) 076012.
- [17] Y.M. Wang, X. Gao, B.L. Ling, et al., *Fusion Eng. Des.* 88 (2013) 2950.
- [18] S.B. Zhang, X. Gao, B. Ling, et al., *Plasma Sci. Technol.* 16 (2014) 311.
- [19] Q. Zang, J.Y. Zhao, L. Yang, et al., *Plasma Sci. Technol.* 12 (2010) 144.
- [20] Q. Zang, J. Zhao, L. Yang, et al., *Rev. Sci. Instrum.* 82 (2011) 063502.
- [21] R.J. Groebner, D.R. Baker, K.H. Burrell, et al., *Nucl. Fusion* 41 (2011) 1789.
- [22] O. Sauter, C. Angioni, Y.R. Lin-Liu, *Phys. Plasmas* 6 (1999) 2834.
- [23] O. Sauter, C. Angioni, Y.R. Lin-Liu, *Phys. Plasmas* 9 (2002) 5140.
- [24] L. Zhang, S. Morita, Z. Xu, et al., *Rev. Sci. Instrum.* 86 (2015) 123509.
- [25] H.Q. Liu, Y.X. Jie, W.X. Ding, et al., *Rev. Sci. Instrum.* 85 (2014) 11D405.
- [26] H.Q. Liu, J.P. Qian, Y.X. Jie, et al., *Rev. Sci. Instrum.* 87 (2016) 11D903.
- [27] C. Zhou, A.D. Liu, X.H. Zhang, et al., *Rev. Sci. Instrum.* 84 (2013) 103511.
- [28] R.R. Dominguez, G.M. Staebler, *Nucl. Fusion* 33 (1993) 51.
- [29] H.R. Du, Z.X. Wang, J.Q. Dong, *Phys. Plasmas* 23 (2016) 072106.
- [30] J.A. Boedo, J. Ongena, R. Sydora, et al., *Nucl. Fusion* 40 (2000) 209.
- [31] M. Murakami, G.R. McKee, G.L. Jackson, et al., *Nucl. Fusion* 41 (2001) 317.
- [32] N. Oyama, A. Kojima, N. Aiba, et al., *Nucl. Fusion* 50 (2010) 064014.
- [33] X.W. Zheng, *The Study of High Plasma Density Experiments on EAST*, PhD Thesis, University of Science and Technology of China, 2016
- [34] J.W. Connor, R.J. Hastie, H.R. Wilson, et al., *Phys. Plasmas* 5 (1998) 2687.
- [35] P.B. Snyder, H.R. Wilson, J.R. Ferron, et al., *Phys. Plasmas* 9 (2002) 2037.

- [36] H.R. Wilson, P.B. Snyder, G.T.A. Huysmans, et al., *Phys. Plasmas* 9 (2002) 1277.
- [37] C.R. Sovinec, A.H. Glasser, T.A. Gianakon, et al., *J. Comput. Phys.* 195 (2004) 355.
- [38] T.Y. Xia, X.Q. Xu, *Phys. Plasmas* 20 (2013) 052102.
- [39] L.L. Lao, H.S. John, R.D. Stambaugh, et al., *Nucl. Fusion* 25 (1985) 1611.
- [40] B.N. Rogers, J.F. Drake, *Phys. Plasmas* 6 (1999) 2797.
- [41] G.T.A. Huysmans, S.E. Sharapov, A.B. Mikhailovskii, et al., *Phys. Plasmas* 8 (2001) 4292.
- [42] R.J. Hastie, P.J. Catto, J.J. Ramos, *Phys. Plasmas* 7 (2000) 4561.
- [43] X.Q. Xu, B. Dudson, P.B. Snyder, et al., *Phys. Rev. Lett.* 105 (2010) 175005.
- [44] D. Banerjee, P. Zhu, R. Maingi, *Nucl. Fusion* 57 (2017) 076005.
- [45] J.A. Crotinger, L. LoDestro, L.D. Pearlstein, A. Tarditi, T.A. Casper and E.B. Hooper, Corsica: a comprehensive simulation of toroidal magnetic-fusion devices. Final report to the LDRD program *LLNL Report UCRL ID-126284*, 1997 (<https://www.osti.gov/servlets/purl/522508>)
- [46] Y. Ye, G.S. Xu, Y.F. Wang, et al., *Nucl. Fusion* 59 (2019) 086044.
- [47] X.Q. Xu, J.F. Ma, G.Q. Li, *Phys. Plasmas* 21 (2014) 120704.
- [48] G.S. Xu, Q.Q. Yang, N. Yan, et al., *Phys. Rev. Lett.* 122 (2019) 255001.
- [49] J. Huang, X. Gong, A.M. Garofalo, et al., *Plasma Phys. Control. Fusion* 62 (2020) 014019.
- [50] R. Nazikian, C.C. Petty, A. Bortolon, et al., *Nucl. Fusion* 58 (2018) 106010.
- [51] Y.F. Wang, H.Q. Wang, G.S. Xu, et al., *Nucl. Fusion* 61 (2021) 016032.
- [52] R. Maingi, D.P. Boyle, J.M. Canik, et al., *Nucl. Fusion* 52 (2012) 083001.
- [53] R. Maingi, S.M. Kaye, C.H. Skinner, et al., *Phys. Rev. Lett.* 107 (2011) 145004.
- [54] C. Giroud, S. Jachmich, P. Jacquet, et al., *Plasma Phys. Control. Fusion* 57 (2015) 035004.
- [55] G.F. Harrer, E. Wolfrum, M.G. Dunne, et al., *Nucl. Fusion* 58 (2018) 112001.
- [56] ITER Organization, ITER Research Plan within the Staged Approach (Level III – Provisional Version), ITER Technical Report, ITR-18-003, 2018 (<https://www.iter.org/technical-reports>)